A&A 677, A36 (2023)
https://doi.org/10.1051/0004-6361/202347089

Astronomy & Astrophysics

Tracing the signatures of a quiet Sun nanoflare

Rebecca A. Robinson[1,2] and Mats Carlsson[1,2]

[1] Rosseland Centre for Solar Physics (RoCS), University of Oslo, PO Box 1029, Blindern 0315, Oslo, Norway
e-mail: rebecrob@uio.no
[2] Institute of Theoretical Astrophysics, University of Oslo, PO Box 1029, Blindern 0315, Oslo, Norway

Received 3 June 2023 / Accepted 13 July 2023

ABSTRACT

Context. Nanoflare-scale reconnection events are difficult to detect, and even when they are detected, it is tricky to reconstruct the details and trigger mechanisms that power them. However, numerical models of nanoflare-scale reconnection can provide context to observations of small-scale reconnection events via the comparison of synthetic observables to observed signatures of the nanoflare.
Aims. We aim to demonstrate how a simulated nanoflare event would look if it were observed by the Solar Dynamics Observatory Atmospheric Imaging Assembly (SDO/AIA) and the upcoming Multi-slit Solar Explorer (MUSE). The goal is to determine the details (if any) of nanoflare-scale reconnection events that could reasonably be captured by current and future instruments.
Methods. We calculated synthetic observables from a quiet Sun simulation of a nanoflare-scale reconnection event, including integrated intensities of Fe IX at 171.073 Å and Fe XII at 195.119 Å. Then, we degraded the synthetic observables to SDO/AIA and MUSE resolutions in order to determine whether the instruments are capable of capturing the details of the reconnection event.
Results. We determine that even small-scale reconnection events in the quiet Sun can be detected by both SDO/AIA and MUSE. In the 171 channel of each instrument, it is possible to discern details of the two bidirectional jets that emanate from the reconnection site. These two bidirectional jets correspond to two different magnetic features undergoing large-angle reconnection with an overlying horizontal field in the corona. In the 193 channel of SDO/AIA, it is only possible to see one set of bidirectional jets, which corresponds to the most energetic reconnecting feature. However, the calculated count rate for AIA 193 is not sufficient for a reliable observation.
Conclusions. Quiet Sun activity is detectable with SDO/AIA and will be detectable with the future MUSE mission. It is possible to detect bidirectional jets with both instruments, which can give context clues as to the mechanisms causing the nanoflare event. The resolution and spectral information of MUSE will give a much more detailed observation of the event, making it much easier to reconstruct a possible trigger mechanism. However, we must be careful in our interpretations of observations when we have limited information, as vastly different physical processes can produce similar observational signatures.

Key words. magnetohydrodynamics (MHD) – magnetic reconnection – Sun: atmosphere – Sun: corona – Sun: UV radiation – Sun: flares

1. Introduction

Solar flares of all sizes, both eruptive and noneruptive, are often associated with instabilities in the solar magnetic field (Priest 1983; Aulanier 2014). When this is the case, magnetic features (e.g., magnetic flux ropes) store magnetic energy before reconnecting with a nearby field, at which point the conversion of magnetic energy to thermal and kinetic energy can power the flare. We know that some flares are too small to scale with the GOES X-Ray Flux solar flare classification system (i.e., A, B, C, M, and X class flares) but that they can still produce enough energy to heat their local atmosphere (Kuhar et al. 2018). This is true even in the quiet Sun, where nanoflares ($\approx 10^{17}$ J) can impulsively heat the atmosphere to over one million degrees (e.g., Parker 1988; Hannah et al. 2011; Hahn et al. 2022; Bakke et al. 2022; Robinson et al. 2022).

These small-scale events are simple enough to simulate, but they are not always easy to observe well enough to understand the underlying magnetic instabilities that power them. Sometimes spanning just a couple of megameters, these events are only large enough to fill a few pixels of full disk images taken by the Solar Dynamics Observatory Atmospheric Imaging Assembly (SDO/AIA; Pesnell et al. 2012; Lemen et al. 2012; Boerner et al. 2012). As such, it can be difficult to justify searching for nanoflare-scale events in observations unless co-observations and simulations can provide context clues as to which magnetic features may be driving them.

As the spatiotemporal resolution of available instrumentation improves over time, small-scale events are becoming significantly easier to detect in multiple wavelengths. There is already a wealth of observations of small-scale reconnection events such as Ellerman bombs (e.g., Zachariadis et al. 1987; Bello González et al. 2013; Libbrecht et al. 2017; Joshi & Rouppe van der Voort 2022), nanoflares (Testa et al. 2013; Ulyanov et al. 2019; Antolin et al. 2021; Bahauddin et al. 2021; Purkhart & Veronig 2022), and the newly observed "campfires" detected by the Extreme Ultraviolet Imager on board the Solar Orbiter (Berghmans et al. 2021; Chen et al. 2021; Kahil et al. 2022), which could potentially be nanoflares themselves.

Such observations of small-scale events are likely to improve with future instruments such as the Multi-slit Solar Explorer (MUSE; De Pontieu et al. 2020, 2022; Cheung et al. 2022). MUSE will use a 37-slit spectrograph to collect the spectra of four prominent extreme ultraviolet (EUV) lines, with the aim to explore the hot transition region and corona in unprecedented detail. The 37 slits will be able to capture simultaneous information over a larger field of view than a single-slit scanner, allowing for the best spatial and temporal resolution yet. These

developments bode well for a bright future of observing small-scale events, and cooperation between these observations and numerical models can help constrain how and why these events occur.

With the numerical tools available, it is possible to use simulations to add an extra dimension to 2D observables and provide their necessary context. By calculating synthetic observables from high resolution MHD simulations and comparing them to what the instruments would be able to see, we can begin to understand how the 3D information would be projected onto a 2D observation, including what is lost, what is preserved, and what is enhanced. Synthetic SDO/AIA and MUSE observations have been calculated for a range of magnetic and energetic events (e.g., Martínez-Sykora et al. 2011, 2018; Hannah et al. 2019; Cheung et al. 2022; Nóbrega-Siverio & Moreno-Insertis 2022). In particular, synthetic MUSE observables have been calculated using several numerical models, including Bifrost simulations of the quiet Sun and coronal holes as well as RADYN simulations of nanoflares (De Pontieu et al. 2022). The specific goal of this work is to zoom in on nanoflare-scale events, in particular magnetic features that are not associated with flux emergence or flux cancellation but instead form and reconnect in the corona.

In this work we discuss a coronal heating event, also described in Robinson et al. (2022), that results in atmospheric plasma temperatures of up to 1.47 MK and an integrated Joule heating energy on the order of 10^{17} J. The event is powered primarily by a magnetic flux rope that self-orders in the corona by way of a series of low-angle reconnections (Robinson et al. 2023). This is the third in a series of papers describing this nanoflare-scale event; the first two deal mostly with the magnetic topology and formation of the event, and this one sets the event into the context of observables. Here, we aim to show how this event would look if it were observed with SDO/AIA and discuss future possibilities for nanoflare-scale observations with the upcoming MUSE instrument.

2. Methods

2.1. The Bifrost simulation

This work focuses on a simulation run with the parallel numerical code Bifrost, which was developed to simulate stellar atmospheres from the convection zone to the corona as detailed in Gudiksen et al. (2011). This fully stratified, 3D magnetohydrodynamics (MHD) model is a laboratory for investigating the plasma and magnetic dynamics of stars and, in this case, the Sun.

The explicit, third-order time stepping recipe in our Bifrost simulation follows the description in Hyman (1979). In the lower chromosphere and upper photosphere, radiative transfer calculations are implemented using a short characteristics scheme following Hayek et al. (2010). These calculations take into account multigroup opacities with four opacity bins (Nordlund 1982) and scattering (Skartlien 2000). In the upper chromosphere, transition region, and corona, the radiative energy budget is solved according to Carlsson & Leenaarts (2012). Conduction along the magnetic field lines in the corona is calculated according to the recipe in Rempel (2017).

The simulation in this work is the same quiet Sun simulation as described in Robinson et al. (2022, 2023). The simulation history is detailed in those references, but we summarize here that we employ a 512^3 Cartesian grid with a thin convective layer, photosphere, chromosphere, transition region, and corona that extends from 2.5 Mm beneath the average $\tau_{500} = 1$ surface (where we define $z = 0$) to 8 Mm above it. Our vertical coordinate is a reference to depth rather than height and therefore, it increases downward from the corona to the convection zone. With that, the vertical component of each vector quantity is aligned accordingly and all 3D renderings in this work reflect that geometry. Vertical spacing is nonuniform; it is sharpest between $z = 0$ and 4 Mm above it, with a grid resolution of 12−14 km. It is most coarse at the upper coronal boundary with a resolution of 70.5 km, and is 30 km at the lower convective boundary.

The horizontal extent of our box is 12 Mm in both horizontal directions with a uniform horizontal grid resolution of 23 km. We use periodic boundary conditions over the horizontal boundaries, which allow us to retain any twist that builds up in cross-boundary magnetic flux ropes (Robinson et al. 2023). The lower convective boundary is open, and allows inflows at a given entropy such that they maintain an effective temperature of ≈5780 K. The upper coronal boundary is left open. We consider hydrogen to be in local thermodynamic equilibrium in this simulation.

In Bifrost, the initial magnetic field is a free parameter and in this simulation, we began our segment of interest with a balanced vertical magnetic field. This field then developed in time via self-consistent convective drivers. In this run, hyper-diffusion terms prevent current sheets that are smaller than the grid resolution and ensure that flux bundles cannot collapse at the numerical resolution (Nordlund & Galsgaard 1995; Gudiksen et al. 2011).

In order to be able to trace specific magnetic field lines and plasma motion in post-processing, we employed a Bifrost module called `corks` (Zacharias et al. 2018; Druett et al. 2022; Robinson et al. 2022, 2023). This module introduces non-interacting Lagrangian markers into the system in order to trace the ideal transport of the plasma as the system evolves. Coordinates and identifications of individual corks were used to understand the magnetic field evolution in Robinson et al. (2022, 2023), and then in this work to understand the plasma velocity in simulated regions of interest.

2.2. Post-processing and analysis

Since we have all of the 3D output from the simulation, we already know what the velocity and temperature distributions are in time and space. With that, only a bit of post-processing was required to pinpoint and isolate any plasma jets emanating from the reconnection event. This was done in bulk as well as for individual test particles, using output from the aforementioned `corks` module. However, the goal of this work is to compare with observations, so instead of plasma velocity, we needed the line-of-sight Doppler velocity that an instrument would see. Instead of temperature, we needed to find the spectral intensity of ions that form at certain temperatures.

In order to do so, we calculated the intensity at each relevant passband using the CHIANTI version 10 database (Dere et al. 1997; Del Zanna et al. 2021). We integrated along two separate axes in order to simulate a top-down, disk center view (z-axis) as well as a side-on, limb view (y-axis) of our nanoflare-scale event. Especially since the jets emanating from the simulated reconnection region are largely horizontal, it was necessary to have at least one horizontal integration in order to get a line-of-sight Doppler velocity along one horizontal component of the jets. We chose two EUV lines as tracers of the nanoflare event: Fe IX at 171.073 Å and Fe XII at 195.119 Å. These two ions are good tracers of quiet Sun activity and can trace temperatures from roughly 800 000 K and higher. Additionally, these two ions

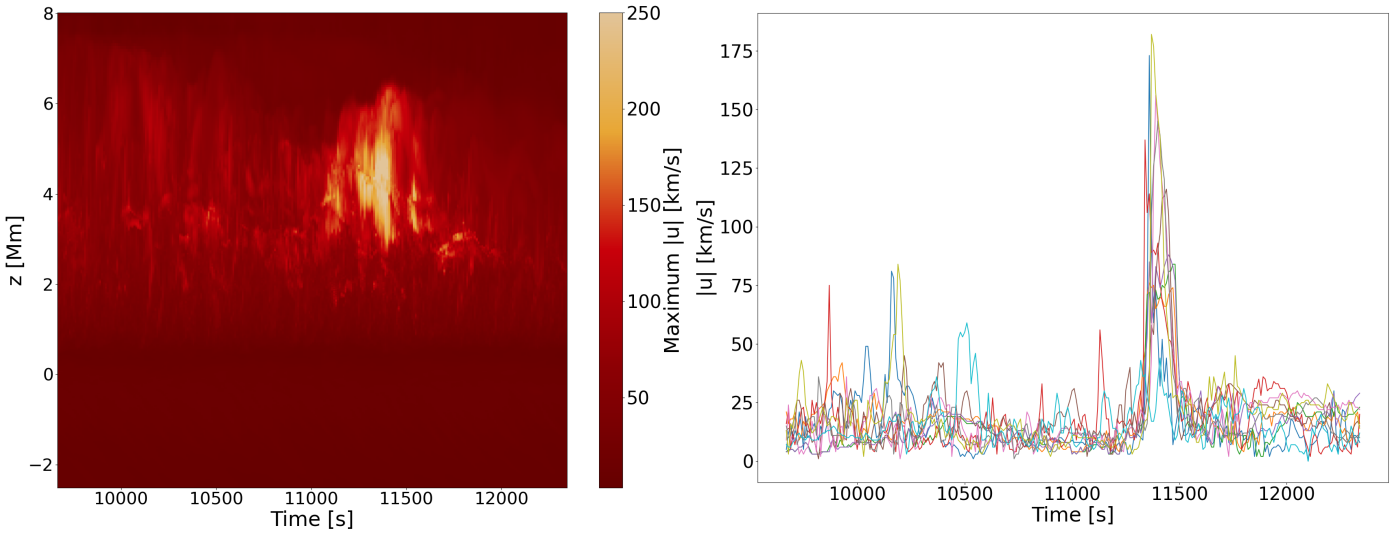

Fig. 1. Time series of the maximum value of the absolute value of the velocity, $|\boldsymbol{u}|$, for each height (left). By selecting certain corks that end up in a jet during the reconnection event, it is possible to follow individual test particles and their associated velocities in time (right).

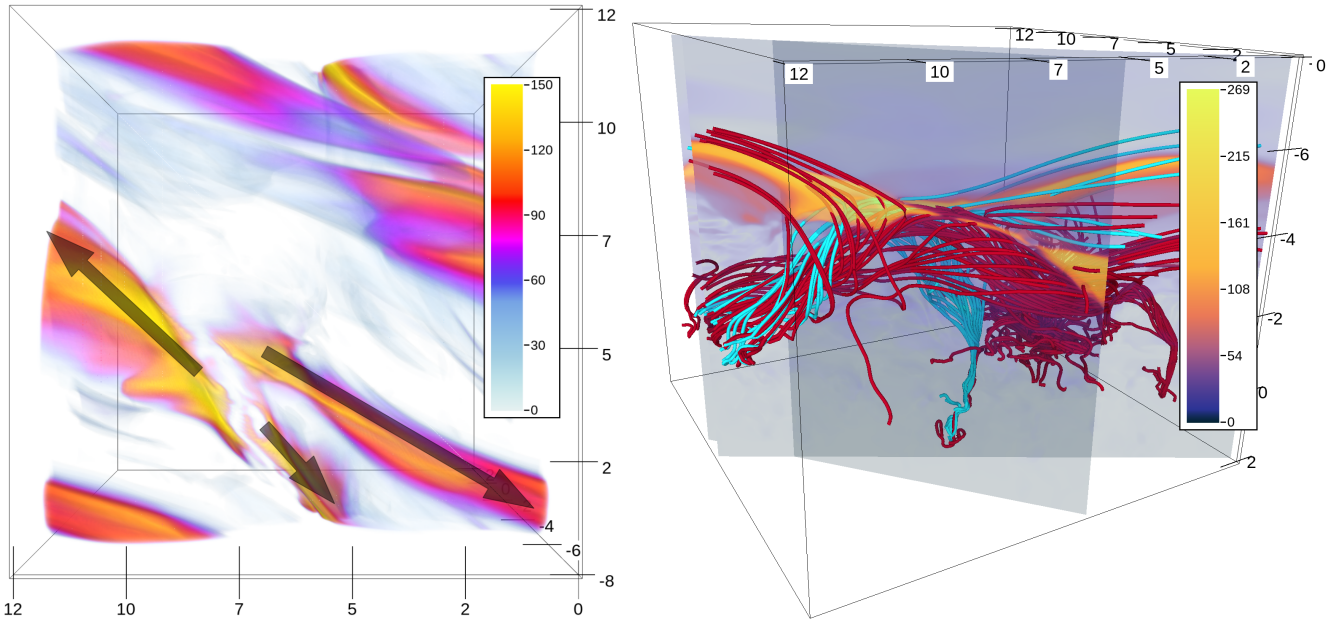

Fig. 2. Top-down volume rendering of $|\boldsymbol{u}|$ at $t = 11\,360$ s (left) with superimposed arrows (black) indicating the direction of flow as the plasma emanates from the reconnection region. The arrows trace two bidirectional jet systems, which breach the periodic boundaries and reenter the box over the corners. The colors of the volume rendering are transparent below $|\boldsymbol{u}| = 10.5\,\mathrm{km\,s^{-1}}$ and saturated (bright yellow) at $150\,\mathrm{km\,s^{-1}}$. The right panel shows a flow rendering of a magnetic arcade (cyan) and a magnetic flux rope (red) at $t = 11\,360$ s. Vertical slices indicate the two bidirectional jet systems that align with the magnetic features, the same systems as those in the left panel. The colors denoting the velocities along each slice are not saturated; the maximum value (brightest yellow) is $\approx 269\,\mathrm{km\,s^{-1}}$.

provide a decent proxy for comparison with SDO/AIA channels 171 and 193 for the same ions, as well as the MUSE 171 channel.

Once the integrated intensities of both ions were calculated in both directions, we extracted the spectral profiles as well as Doppler velocity maps. Integrated intensities were converted to SDO/AIA counts using the instrument response functions at both wavelengths, and then degraded to a pixel resolution of 0.6″ (Boerner et al. 2012). MUSE synthetic intensities were calculated by folding the velocity differential emission measure (VDEM) with the MUSE 171 response function and degraded to the highest possible spatial resolution of 0.167″ (De Pontieu et al. 2022). Then, we could compare the "ground truth" simulation results to what AIA 171, AIA 193, and MUSE 171 would see if these instruments were to observe our simulated nanoflare event.

3. Results

3.1. Plasma properties

The geometry of the main magnetic reconnection event has been discussed in Robinson et al. (2022) in terms of magnetic topology, but here we describe the associated plasma properties. In Robinson et al. (2023), we discussed the buildup of magnetic

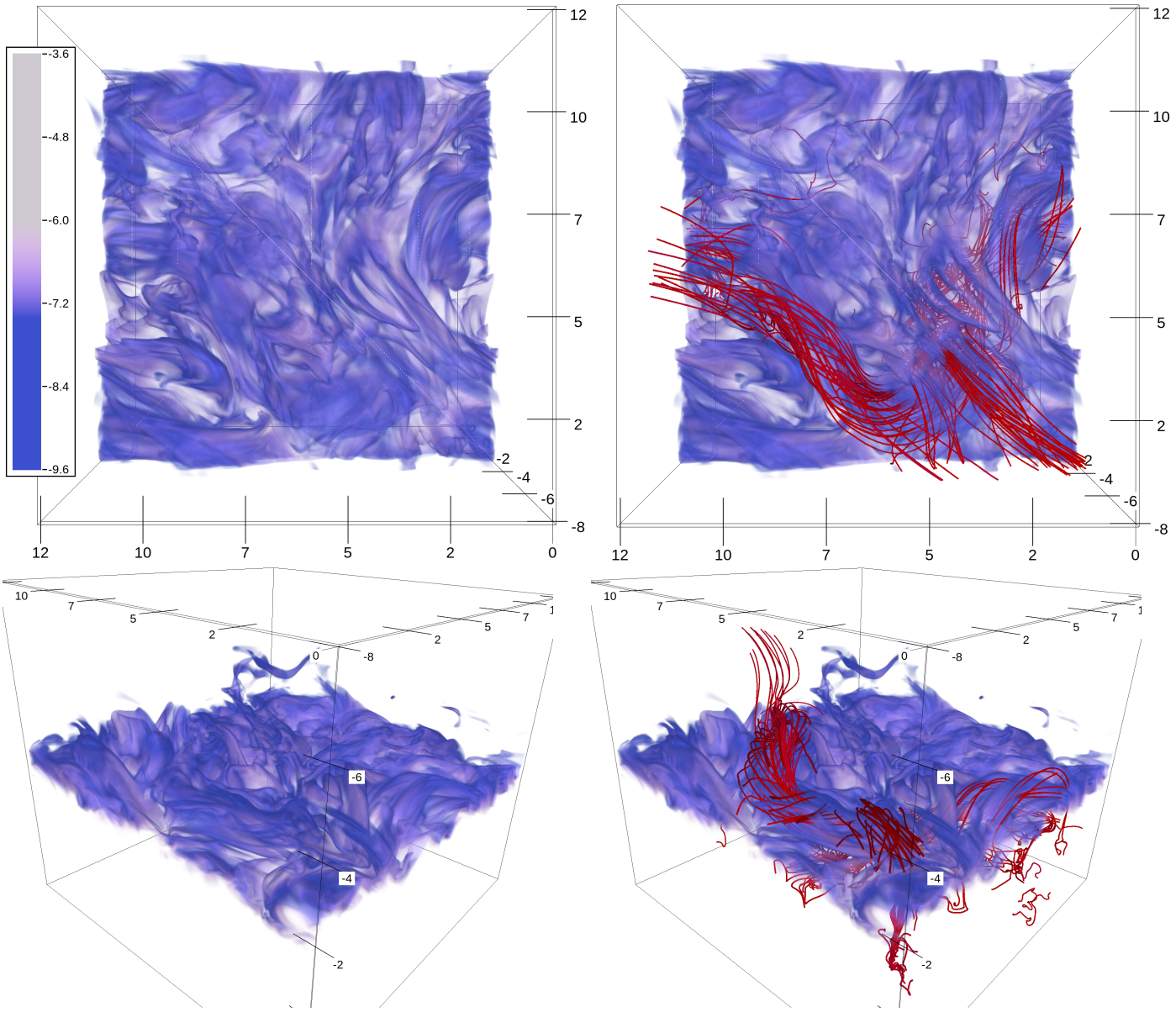

Fig. 3. Volume renderings of chromospheric density fluctuations (log ρ) at $t = 11\,360$ s. All densities higher than log $\rho = -3.6$ and lower than log $\rho = -9.6$ are transparent. This means that the gray plasma is under-dense compared to the transparent plasma beneath it, and the blue plasma is over-dense compared to the transparent coronal plasma above and around it. The left two panels do not include magnetic flux rope field lines whereas the right two panels do, illustrating that an over-dense mini-filament in the chromosphere is aligned well with the non-reconnecting lines of the magnetic flux rope at that time. The magnetic field lines therefore act as a guide for identifying the mini-filament.

energy that ultimately powers this nanoflare event. Due to the transfer of magnetic energy to thermal and kinetic energy, we expect to see fast plasma jets upon reconnection. The left panel of Fig. 1 illustrates a time series of the maximum value of plasma velocity $|\boldsymbol{u}|$ for each height. As expected, we see fast plasma during the major reconnection event between 11 200 s and 11 500 s.

In Robinson et al. (2022, 2023), we described the use of corks as Lagrangian markers for the purpose of tracing consistent magnetic field lines through the simulation. It is also possible to use them to trace plasma velocity at particular points. By following select corks that eventually end up in the plasma jets, we can clearly see their velocity evolution as shown in the right panel of Fig. 1. Each colored line represents the speed of one cork over the time span of the simulation, and during the major reconnection event between 11 200 s and 11 500 s, we see a rapid acceleration and deceleration of the corks as they enter and exit the plasma jets.

During the nanoflare-scale reconnection event, we see that there are two systems of bidirectional jets emanating from the reconnection region. This is because there are two separate magnetic features that reconnect with the overlying coronal field as discussed in our previous works. One system of bidirectional jets is associated with a magnetic arcade, and the other is associated with a magnetic flux rope. The left panel of Fig. 2 shows a top-down view of the bidirectional jet systems at $t = 11\,360$ s, with black arrows indicating the direction of the plasma. We note that the high velocity jets in the corners of the box are a result of our periodic boundary conditions; they have reentered the box after initially leaving the reconnection site.

As established in Robinson et al. (2022) and mentioned above, the two most relevant magnetic features that contribute

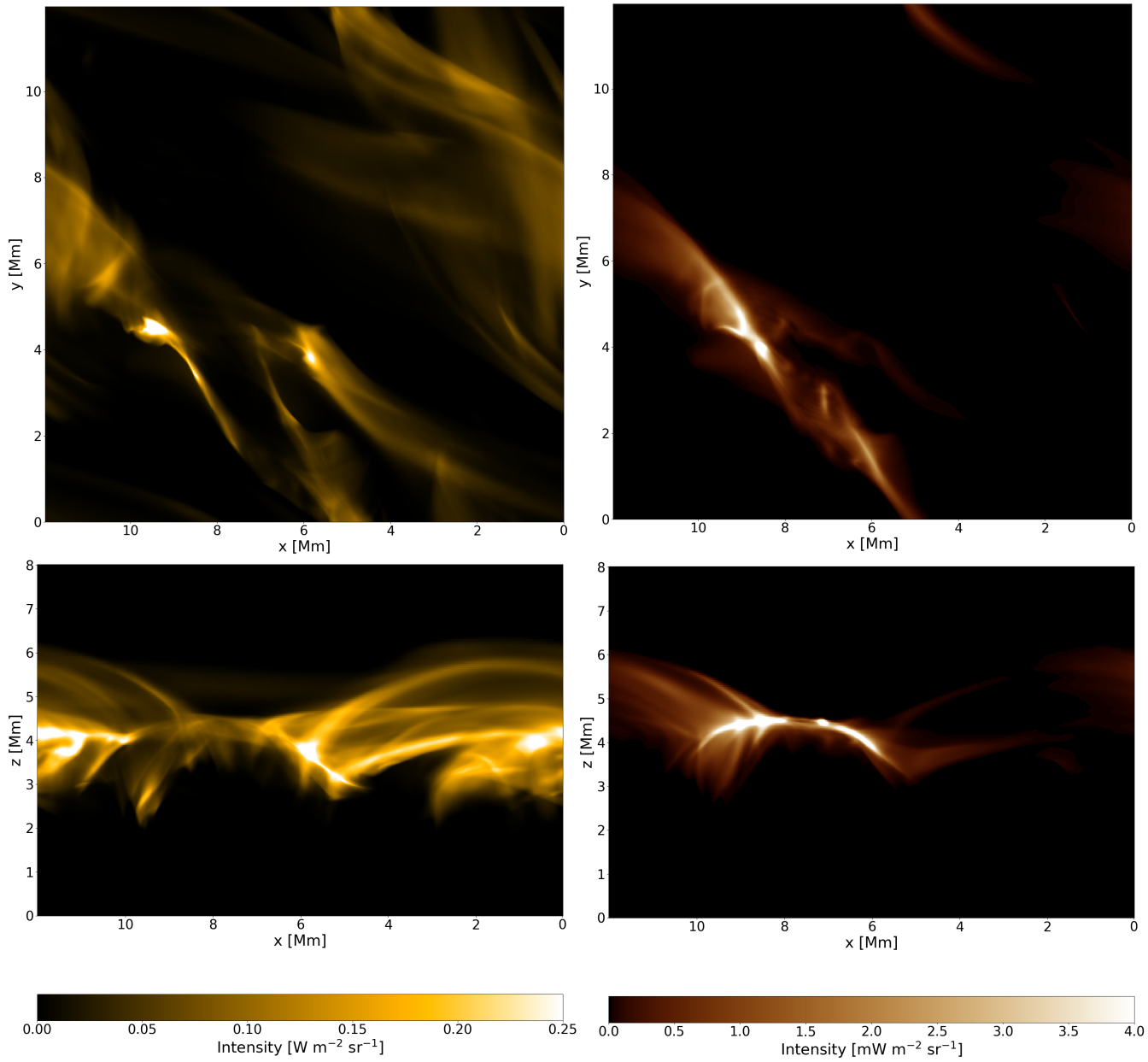

Fig. 4. Synthetic integrated intensities at $t = 11\,360$ s integrated along the z-axis (upper) or y-axis (lower) for Fe IX 171 Å (left) and Fe XII 195 Å (right). These intensities are shown at the native resolution of the simulation.

to the nanoflare event are a magnetic arcade and a magnetic flux rope, which reconnect with an overlying horizontal field. The right panel of Fig. 2 illustrates the flux rope (red) and arcade (cyan) field lines as well as two 2D vertical slices showing the plasma velocity through each jet system at $t = 11\,360$ s. It is clear that reconnecting lines from the arcade (cyan) and flux rope (red) are associated with the two bidirectional jet systems. On the left side of the reconnection region, the arcade and flux rope are tangled around one another and the bulk plasma jet there is associated with those lines. On the right side, the short jet is most associated with the flux rope lines, while the longer jet is most associated with the arcade lines. This illustrates how a multi-jet system can be associated with multiple magnetic features undergoing large-angle reconnection.

The fast plasma jets are associated with the proper reconnection site and therefore associated with the hottest plasma, meaning they would be visible in optically thin coronal lines. However, it is also possible to see the lower flux rope down in optically thick layers, because signatures of the flux rope can be seen via density fluctuations. We do not discuss synthetic observations of optically thick lines, but we would like to show how the magnetic flux rope in particular could be identified.

Figure 3 shows how the lower, non-reconnecting parts of the flux rope can be seen in density fluctuations lower in the atmosphere. Each panel shows a volume rendering of the log of density at $t = 11\,360$ s near the height of the flux rope, illustrating that the flux rope can be seen as a slightly over-dense structure. We note that the magnetic flux rope lines can be used as a guide to trace the structure, as they wind through it. This suggests that it could be possible to observe signatures of a non-reconnecting flux rope even though there is not much thermal energy at lower layers. Figure 3 also indicates that a slightly over-dense region in

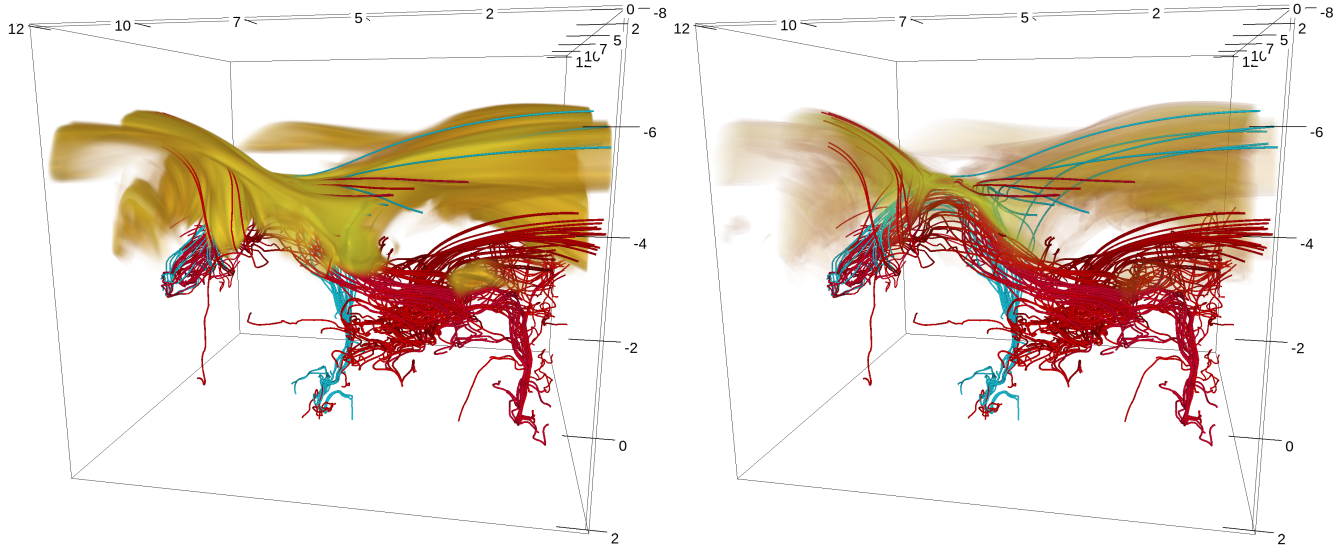

Fig. 5. Volume renderings of temperature and reconnecting magnetic features at $t = 11\,360$ s. The temperature opacity function follows the response functions of AIA 171 (left) and AIA 193 (right).

the chromosphere may resemble a mini-filament following the geometry of the flux rope. It is in this manner that flux ropes in the quiet Sun could be detected; that is, by detecting mini- or micro-filaments (Sterling & Moore 2016; Hong et al. 2016; Sterling et al. 2020; Syntelis & Priest 2021). A full discussion of mini-filaments is beyond the scope of this analysis, but our ability to see the flux rope as a density structure and possible mini-filament is worth mentioning because it could provide clues toward understanding which magnetic features are most relevant to the reconnection. In the rest of this report, we discuss optically thin EUV lines that form in the reconnection region itself, which help us understand how EUV-detecting instruments could observe an event such as our simulated nanoflare-scale reconnection event.

3.2. Synthetic observables

In order to compare our simulation to possible observables, we calculated integrated intensities for select EUV lines. The intensities for both Fe IX 171.073 Å and Fe XII 195.119 Å were integrated along the z-axis for a top-down view, or the y-axis for a limb view of the heating event. Figure 4 illustrates the integrated intensities for both lines, integrated in both directions.

The left panels of Fig. 4 show the integrated intensities for Fe IX 171 Å at $t = 11\,360$ s. Most notably, the top-down integration (upper-left) shows the two systems of bidirectional jets, as previously seen in Fig. 2. This is reflective of the two magnetic features that reconnect during this time, meaning that an observation of this type would indicate reconnection between multiple features. The side integration (lower-left) shows an outline of the reconnection X line and emanating jets, but one must be careful when interpreting side integrations of a simulation with periodic boundary conditions. At this snapshot, cross-boundary jets have already appeared and likely make slight contributions to the integrated intensity.

The right panels of Fig. 4 show the integrated intensities for Fe XII 195 Å at the same time stamp. Integrating the intensity of this line will pick out some of the hottest plasma in our simulation; as the maximum temperature during the reconnection event was 1.47 MK, we expect to see a strong signal in the spine of the reconnection region. This is easily seen from both the top-down (upper-right) and side (lower-right) integrations. We note that only the strongest of the bidirectional jet systems is visible in Fe XII 195 Å, which is associated with the magnetic flux rope.

To compare the 2D integrated intensities back to the 3D simulation, we used the response functions of AIA 171 and AIA 193 to determine their 3D distributions in our computational box. Figure 5 shows two temperature renderings overlying the magnetic field lines of the two main features at $t = 11\,360$ s. The left panel shows a volume rendering of temperature where the opacity function of the renderer follows the response function for AIA 171. The right panel is the same, except the opacity function follows the response function for AIA 193. We note that the rendering following the response of AIA 171 (left panel) includes some contributions from cross-boundary jets, whereas the response of AIA 193 highlights mainly the reconnection region. Cross-boundary jets are still present in AIA 193, but the region most opaque and responsive to this wavelength is the reconnection site itself. This illustrates why it is important to understand the 3D context of the 2D synthetic observables; clearly, some cross-boundary jets are contributing to the 2D intensity, which would be most prominent in the lower-left panel of Fig. 4.

To understand the spectral signatures of the plasma velocity and temperature at this time stamp, the first moment of the synthetic spectra were also calculated. Figure 6 gives top-down (upper) and side (lower) views of the Doppler shifts for Fe IX 171 Å at $t = 11\,360$ s. The upper panel shows significant flows in the reconnection region, and the lower panel shows the bidirectional jets. We note that some of these jets are cross-boundary jets, as expected due to periodic boundary conditions. Figure 7 gives the spectral profiles along $x \approx 4$ Mm and 8 Mm, illustrating how different the spectra can be for pixels in different jet systems. The magenta profiles show the spectra near the center of the reconnection region, where both jet systems are released. Above the reconnection region, this cut also captures contributions from a cross-boundary jet behind the reconnection region (see the left panel of Fig. 5). The cyan profiles show contributions from the reconnection jets as well as a cross-boundary jet. While many of the profiles are approximately Gaussian, there

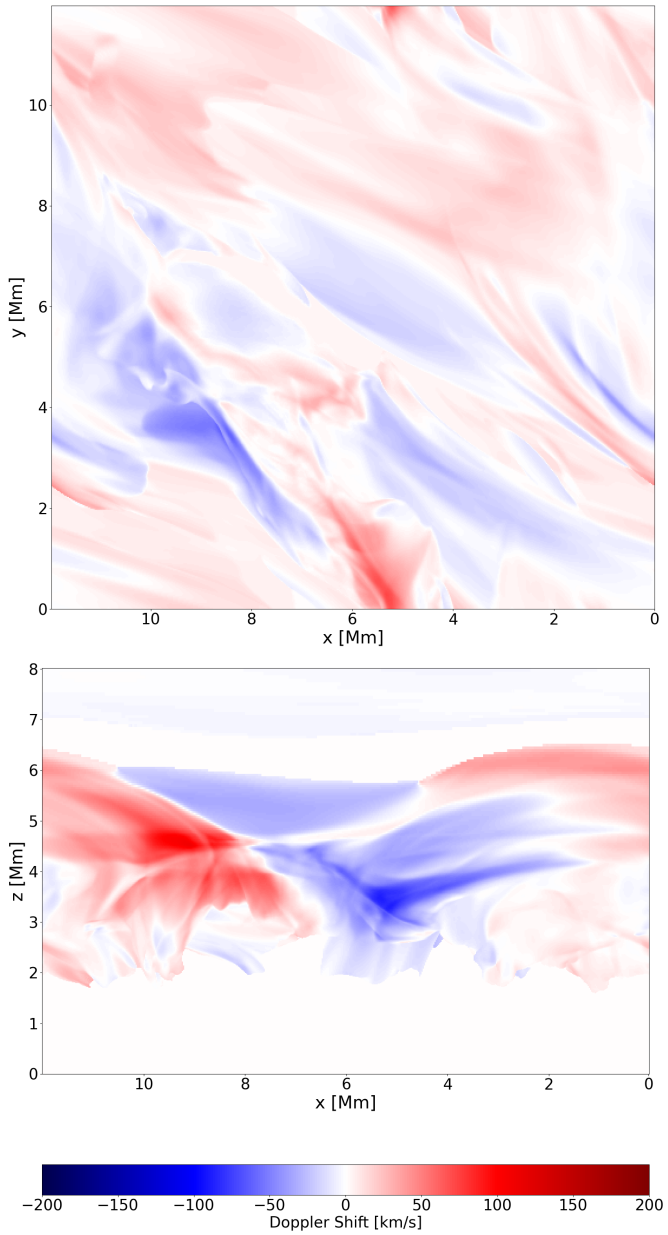

Fig. 6. First spectral moment of the Fe IX 171 Å spectra at $t = 11\,360$ s, representing Doppler shifts along the z-axis (upper) or the y-axis (lower). These Doppler shifts are shown at the native resolution of the simulation.

are also several non-Gaussian profiles that may be a result of several contributions at that pixel.

The nanoflare-scale event gives clear signals in integrated intensities for Fe IX 171 Å and Fe XII 195 Å, as well as sufficient plasma velocities to be seen as clear Doppler shifts in Fe IX 171 Å spectra. Now, we address whether or not SDO/AIA would be capable of capturing a reasonable signal in its 171 and 193 channels, and whether or not MUSE could observe such intensities and Doppler velocities in its 171 channel.

3.3. SDO/AIA

In order to determine the type of signal that could be gathered by SDO/AIA, we converted the synthetic intensities into SDO/AIA counts and degraded the grid resolution to the instrument's pixel resolution 0.6″ as per Boerner et al. (2012). Figure 8 shows a comparison between the "ground truth" synthetic intensities in physical units (left panels) and the intensities after conversion and degradation (right panels) for the 171 channel of SDO/AIA. The top panels are top-down integrations along the z-axis, and the bottom panels are side integrations along the y-axis. The overlying annotations (red circles and arrows) show features of interest. The two bright points in the upper-left panel are well matched in the SDO/AIA degradation, and they make useful reference points for the two bidirectional jets as discussed above and shown in Fig. 2. The red arrows show the direction of flow with respect to the reconnection region and trace the two clear jet systems. This means that, even at SDO/AIA resolution, multiple bidirectional jets can be observed. We note again that the upper-right corner is a cross-boundary jet, and is not considered for this analysis.

The three bright regions in the bottom left panel of Fig. 8 are also seen in the SDO/AIA degradation in the bottom right panel. These bright regions represent warm plasma around the reconnection region, but this wavelength is not as sensitive to the reconnection region itself. Again, we see enhancements in the bidirectional jets but are not able to garner any 3D information from it. We know from the left panel of Fig. 5 that cross-boundary jets in the simulation are likely to contaminate synthetic observables at 171 Å. For this reason, the intensities shown in the lower-right panel of Fig. 8 are slightly enhanced by such cross-boundary jets, and the outline of the reconnection region is clear even with the degradation.

Figure 9 is the same as Fig. 8, but for the 193 channel of SDO/AIA. Again, the upper panels show the top-down integration, where the reconnection X line and the strongest bidirectional jet is marked with a red circle and arrows indicating the direction of flow. It is clear from the upper-right panel that the X line and jets can also be seen in the SDO/AIA degradation. The bottom panels demonstrate that not only is the 193 channel appropriate for tracing the hottest plasma at the X line, but that the X line can still be seen in the SDO/AIA degradation. However, the count rate is not high enough to claim that SDO/AIA can observe the nanoflare event (Boerner et al. 2012), at least at the Fe XII wavelength we selected to compare with the AIA 193 channel. At this wavelength, the maximum count rate for the synthesized 193 channel is 0.33 DN pix^{-1} s^{-1}, which is much lower than expected for such an event. We also note that there is not much corona in our simulation, so we do not expect to see as many counts from the simulation as SDO/AIA would observe.

The count rates calculated for AIA 193 with Fe XII 195 Å are insufficient for reliable detection, but the count rates calculated for AIA 171 with Fe IX 171 Å are sufficient. They are still lower than expected, and are more comparable with coronal hole observations in AIA 171 (Boerner et al. 2012). Again, this could be due to the amount of corona that we have in our simulation, but the event is still detectable. Although details are lost in the degraded synthetic observables, we see from Fig. 8 that our simulated nanoflare event is neither too small nor too weak to be observed with the AIA 171 channel.

3.4. MUSE

MUSE is a future mission that will use a 37-slit spectrograph to simultaneously obtain the EUV spectra of four different EUV lines, including Fe IX 171 Å (De Pontieu et al. 2020, 2022; Cheung et al. 2022). As MUSE is on track to have the highest spatial and temporal resolution yet, it is interesting to explore its predicted sensitivity to our nanoflare event. We note that we only

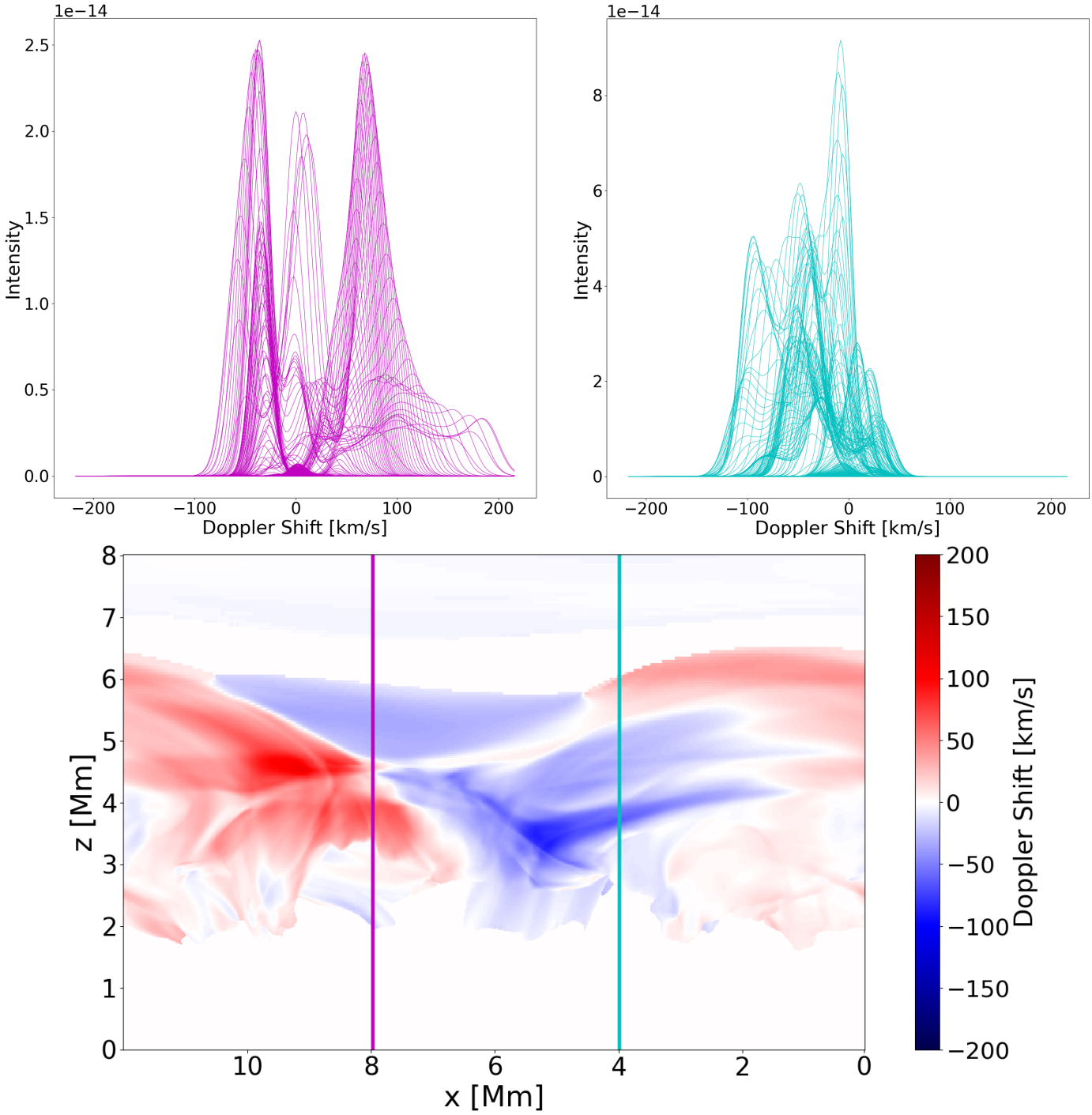

Fig. 7. Spectra along vertical cuts at $x \approx 4$ and 8 Mm at $t = 11\,360$ s. The upper-left panel is a collection of spectra along $x \approx 8$ Mm, and the upper-right panel is the spectra along $x \approx 4$ Mm. For reference, the lower panel shows the Doppler shift as well as the locations of the cuts.

explore the spatial and spectral resolution of MUSE and consider only one time stamp for this analysis. Indeed, the temporal resolution of MUSE would be sufficient to observe the bidirectional jets, as these last longer than one minute in the simulation and spatially extend across just tens of megameters. A full, time-dependent MUSE synthesis is beyond the scope of this study, but would be an interesting and instructive next step.

The left panels of Fig. 10 show the synthetic intensity of Fe IX 171 Å in physical units, and the right panels show the intensity folded through the MUSE response function and degraded to a resolution of 0.167″. Realistically, MUSE resolution is $0.4'' \times 0.167''$, but as the slits can observe features at any angle, it is instructive to illustrate the capabilities of MUSE by showing images at a uniform $0.167'' \times 0.167''$ resolution. This way, synthetic images show the finest possible features detectable by MUSE. Our synthetic MUSE count rates are comparable to those reported in De Pontieu et al. (2022) for RADYN nanoflare simulations `E2` and `H1` (Polito et al. 2018; Testa et al. 2020), which further solidifies the conclusion that MUSE is capable of observing nanoflare-scale events in detail.

A comparison of Figs. 8 and 10 illustrates how synthetic MUSE 171 observations look in contrast to synthetic AIA 171

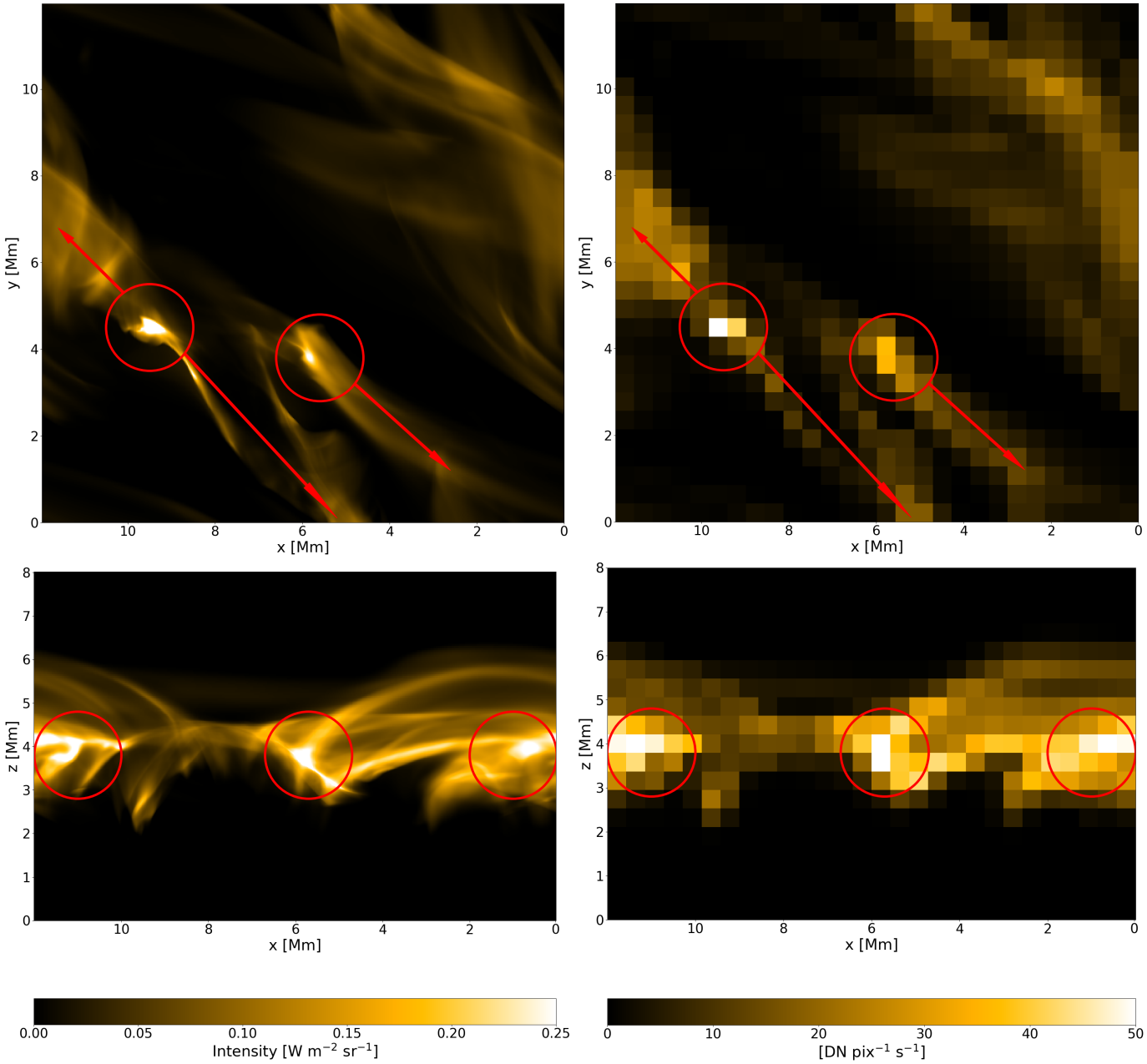

Fig. 8. Original synthetic intensities for Fe IX 171 Å (left) compared to synthetic AIA 171 observations (right) at $t = 11\,360$ s. Bright points of interest are denoted with red circles, and the two jet systems in the upper panels are denoted with red arrows. Synthetic AIA 171 images have a pixel resolution of 0.6″.

observations. Very similar features are visible for the top-down (upper panels) and side integrations (lower panels) but it is clear that MUSE can do a much better job resolving the two bidirectional jet systems. Comparing the right panels of both figures, it is evident that while the jets are still visible in AIA 171, their details are much easier to discern with the high spatial resolution of MUSE 171.

From Figs. 6 and 7, we know that the simulated reconnection event is dynamic with high velocity, bidirectional jets. Therefore, spectral information is crucial to understand the underlying physics. MUSE is designed to provide this information at the required spatial, spectral, and temporal resolution. With that, we use our synthetic observables to see how this spectral information would look with MUSE if it were to observe our nanoflare-scale event. The first spectral moment is shown in Fig. 11 for top-down (upper) and side (lower) integrations. These figures show pixels only where the MUSE intensity count rate is higher than 5 DN pix^{-1} s^{-1}, because pixels contaminated with too much photon noise are not reliable enough for calculating the first spectral moment. Comparing Figs. 6 and 11, we can see that both Doppler maps feature similar bidirectional jet systems, as expected for the spatial resolution of MUSE.

Now, the question is whether or not the spectral resolution of MUSE is sufficient to reproduce the spectra in Fig. 7. The upper panels of Fig. 12, similar to Fig. 7, show a collection of spectra at $x \approx 4$ Mm and 8 Mm, at the MUSE spectral resolution of 14.6 mÅ, which translates to 25.6 km s^{-1}. At this spectral resolution, the spectra are comparable to the most prominent

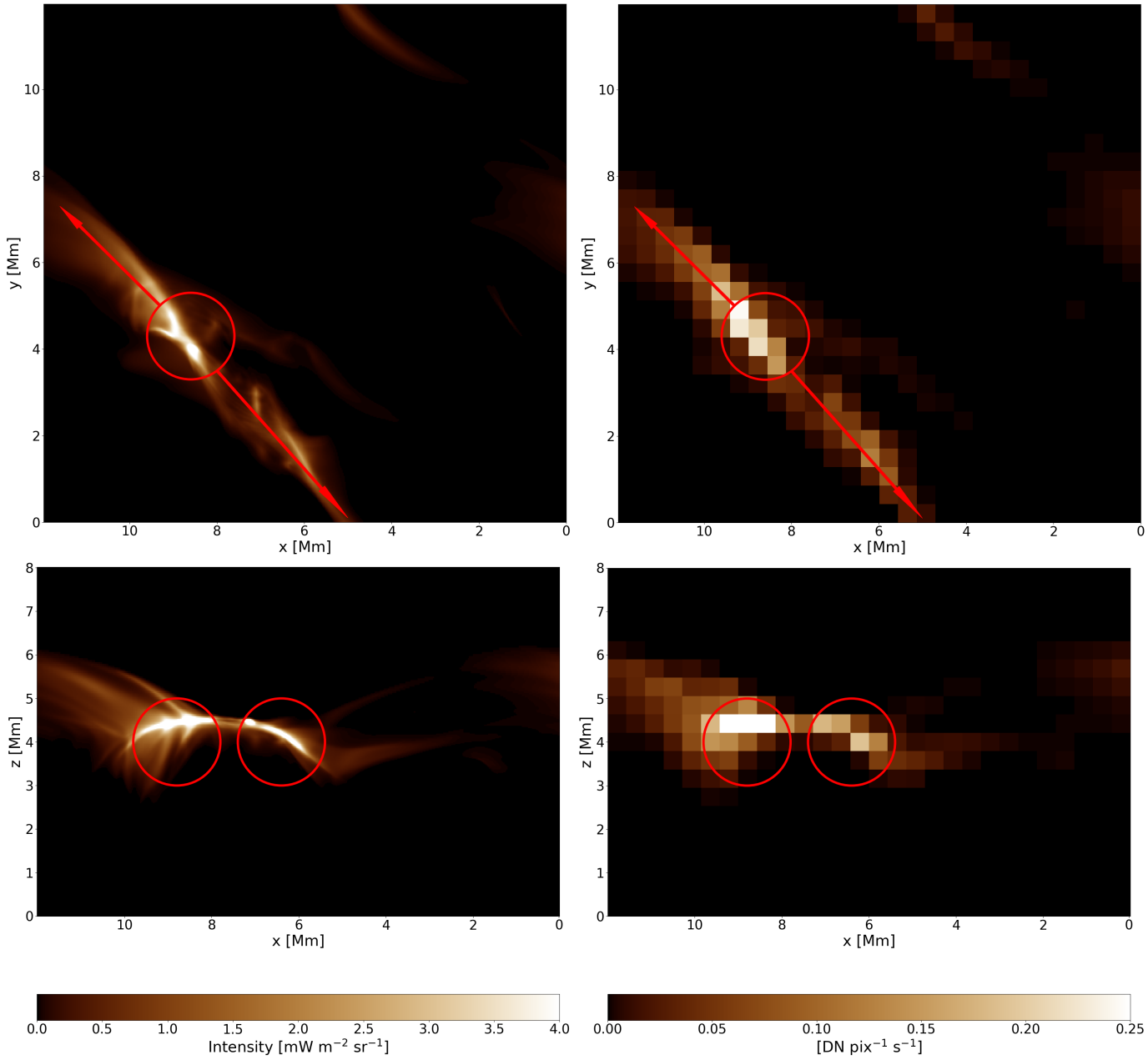

Fig. 9. Original synthetic intensities for Fe XII 195 Å (left) compared to synthetic AIA 193 observations (right) at $t = 11\,360$ s. Bright points of interest are denoted with red circles, and the one detectable jet system is denoted with red arrows in the upper panels. Synthetic AIA 193 images have a pixel resolution of 0.6″.

features in Fig. 7, but cannot capture the weaker features. The magenta spectra at $x \approx 8$ Mm display both blue- and redshifts, cutting through jets flowing in opposite directions, and peaking at approximately the same values as in Fig. 7. The cyan spectra at $x \approx 4$ Mm are primarily blueshifted, but the MUSE spectral resolution cannot capture the details seen in Fig. 7. The clearly redshifted spectra in Fig. 7 are not fully present in Fig. 12; any redshifted spectra appear broadened and flattened due to the coarser spectral resolution of MUSE, as well as the pixel intensity cutoff at 5 DN pix^{-1} s^{-1}. Overall, the MUSE spectra are generally broader compared to the original synthetic spectra, but again, this is a result of the coarse spectral resolution. Even with the loss of detail, we conclude that MUSE would be able to reliably observe bidirectional jet systems in a nanoflare-scale event, both spectrally and spatially.

4. Discussion

4.1. Setting synthetic observables in context

We have now established that the 171 channels of both SDO/AIA and MUSE would be capable of capturing a nanoflare-scale reconnection event in the quiet Sun. Here, we briefly discuss what those observations may be able to tell us. In Robinson et al. (2022, 2023), we discussed the formation and onset of such a reconnection event in our quiet Sun simulation. The first study determined that impulsive heating occurs because a magnetic flux rope and magnetic arcade reconnect with an overlying, nearly antiparallel horizontal field in the corona. The second study provides an explanation for the formation of the flux rope over time via the inverse cascade of helicity. With this

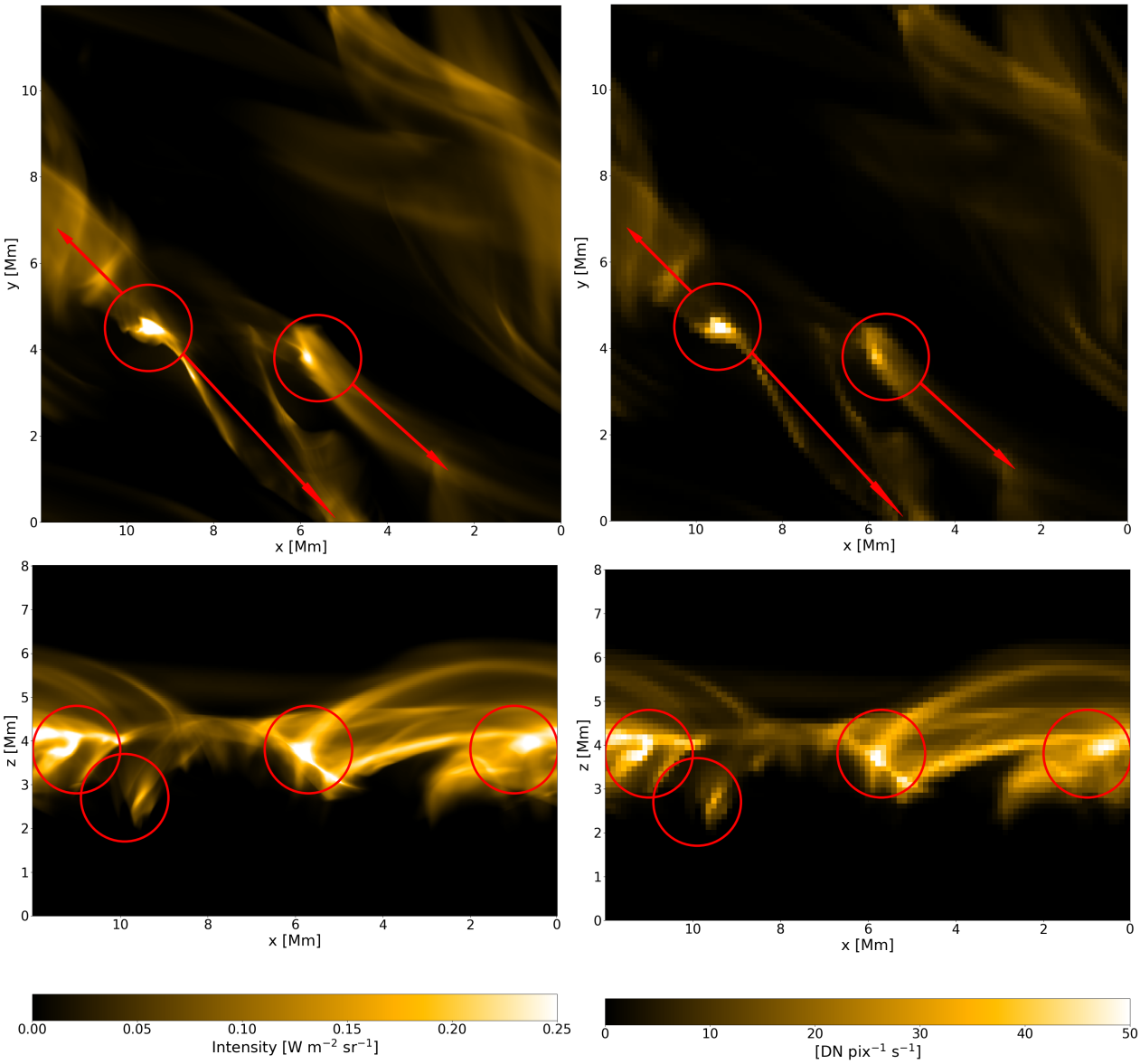

Fig. 10. Original synthetic intensities for Fe IX 171 Å (left) compared to synthetic MUSE intensities (right) at $t = 11\,360$ s. Bright points of interest are denoted with red circles, and the two jet systems in the upper panels are denoted with red arrows. Synthetic MUSE observations are degraded to the highest possible resolution of 0.167″.

information, we have a functional understanding of how the flux rope forms, stores magnetic energy, and ultimately powers the heating event.

Within that context, synthetic observables can shed light on what such processes may look like observationally. In this case, we provide an example of flux rope formation in the corona; not an example of flux emergence through the atmosphere. Knowing this, the observational signatures of such an event are not linked to coherent flux emergence but, rather, flux rope formation and eventual major reconnection in the corona.

Because of this, it is worth mentioning that a photospheric magnetogram can only help contextualize observations of this type of event by providing information about the average background field, and ruling out any connection to traditional convective processes in the photosphere. Usually, it is helpful to align an atmospheric observation with its corresponding magnetogram in order to trace any relevant photospheric roots involved in flux cancellation or flux emergence. In this case, and as discussed in detail in Robinson et al. (2022), the photospheric roots of the relevant magnetic features do not undergo relevant flux cancellation. Additionally, as shown in Robinson et al. (2023), the relevant features form in the corona via low-angle reconnection and do not emerge coherently through the photosphere. For these reasons, any associated photospheric magnetogram would not be helpful for reconstructing the relevant processes that power this nanoflare event. Although the event is ultimately driven by convective drivers, the effects of those drivers are not so obvious in the photosphere as they are in the upper atmosphere. Traditional methods of cross checking atmospheric observables with a photospheric magnetogram are therefore not helpful for finding signatures of self-ordered coronal flux ropes undergoing reconnection with overlying fields, except to rule out flux emergence or cancellation.

Without a magnetogram as a guide, we must look for other clues in the observables that we can expect from such an event. It is helpful to have access to the 3D information provided by

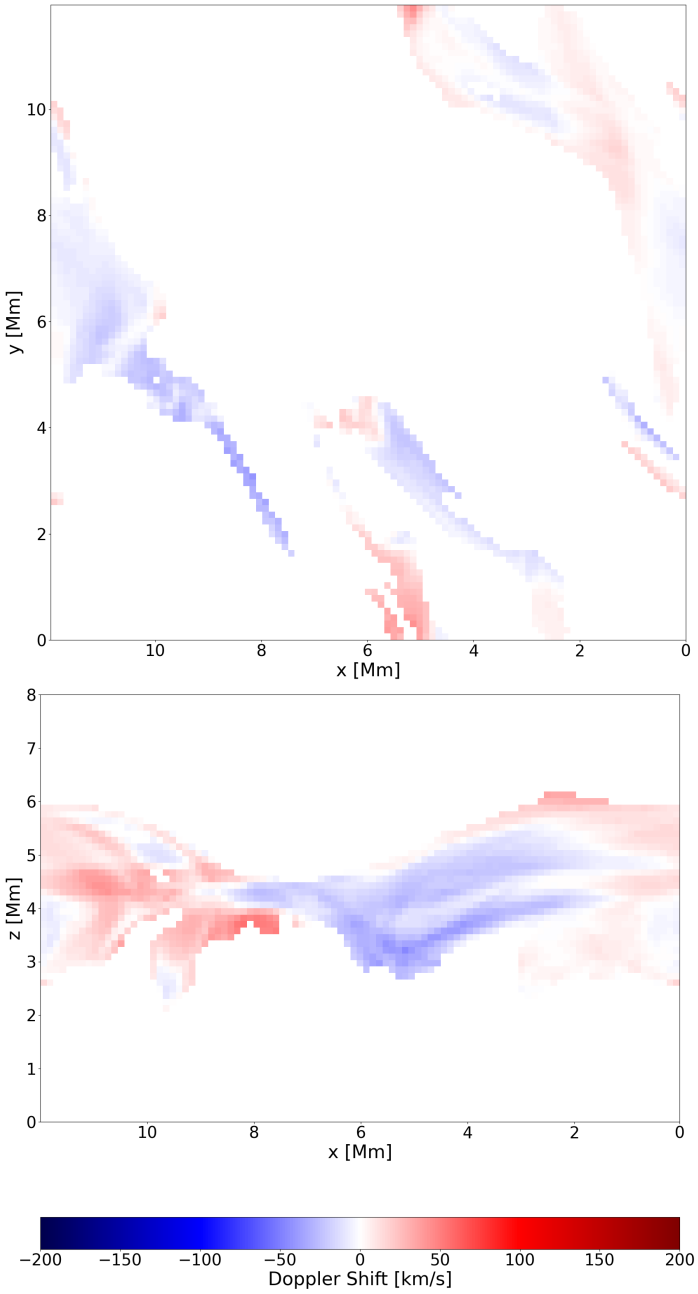

Fig. 11. MUSE synthetic Doppler shifts at $t = 11\,360$ s. Pixel intensities greater than 5 DN pix^{-1} s^{-1} have been degraded to the MUSE pixel resolution of 0.167″. The upper panel shows the Doppler shift along the z-axis, and the lower panel shows the Doppler shift along the y-axis.

the simulation, as observations are 2D representations of many possible 3D processes. In our case, we see the 2D projection of one known 3D process when we compute synthetic observables, and that 3D ground truth is not necessarily the simplest possible case. At first glance, it may seem nearly impossible to be able to reconstruct our 3D situation out of the 2D synthetic observables generated by it; with too many degrees of freedom and possible outcomes, it would require some degree of creativity to reconstruct our 3D simulation. However, there are a number of clues in our various observables that, without having access to any 3D information, may point an observer in the right direction.

One such clue is the fact that we have two separate, yet intertwined, systems of bidirectional jets. This can be seen in our synthetic observations of Fe IX 171 Å, where two clear jet signals emerge from the reconnection site as in the upper-left panel of Figs. 4, 8, and 10. Since we know that our bidirectional jets each belong to a reconnecting magnetic feature in the simulation, seeing this in the synthetic observables indicates that two different magnetic features may be in the process of reconnecting with an overlying field. The information essentially stops there, though; without the simulation, it is not possible to determine whether the magnetic features are a sheared arcade and a flux rope as in our situation, or something entirely different.

It is notable, though, that only one set of bidirectional jets can be seen in our synthetic intensities of Fe XII 195 Å, in the upper-right panel of Fig. 4. This is because the hottest, most energetic plasma is released along the jet most aligned with the flux rope, which has had the time to build up significant magnetic energy before reconnection (Robinson et al. 2023). Comparing the intensities of Fe IX and Fe XII could help determine how many reconnecting features there may be, and then which of them is the most energetic reconnecting feature; that is, as long as Fe XII is also detectable. We have now seen that the bidirectional jet features are visible in AIA 171 (see Fig. 8) and MUSE 171 (see Fig. 10), meaning that both instruments could be used to detect large-angle reconnection between multiple magnetic features in the quiet Sun. The most notable part of this is not only that both instruments could be used to detect the reconnection event, but that both instruments have the capability to discern that more than one magnetic feature may be involved.

Another clue to what is happening is the over-dense areas of the chromosphere that correspond to the parts of the magnetic flux rope that lie underneath the reconnection region. In terms of density fluctuations, the flux rope sits atop the rest of the plasma, resembling a mini-filament that could be observed in optically thick lines (see Fig. 3). Co-observing with optically thin lines may be helpful, because if coronal heating is seen in the optically thin lines and the optically thick lines trace an over-dense mini-filament in the chromosphere, it is possible that the mini-filament is contributing to the coronal heating by way magnetic energy storage and release. In our case, the flux rope powers the reconnection event due to the buildup of magnetic energy via component reconnection (Robinson et al. 2023). Co-observing both optically thin and optically thick lines could make it possible to reconstruct not only a heating event, but the feature(s) that are powering the event.

4.2. Comparison to earlier observations

The High-resolution Coronal Imager (Hi-C) completed a successful mission on 11 July 2012 that includes Fe IX 171 Å and Fe XII 193 Å observations of magnetic braiding in the corona (Cirtain et al. 2013). These observations appear to be especially similar to the upper-right panel of Fig. 4. The Hi-C observations and our synthetic observations, however, are results of two very different physical processes. The result of the Hi-C campaign is the first evidence-based observation of magnetic braiding in the corona, characterized by a clear X line shape seen in Fe IX 171 Å and Fe XII 193 Å. We also see a clear X line especially in our Fe XII 195 Å synthetic observation, but we see this brightening as a result of large-angle reconnection between the magnetic flux rope, arcade, and horizontal coronal field (Robinson et al. 2022). Ours is certainly not low-angle component reconnection as seen in the Hi-C results, as component reconnection in our simulation cannot produce such high temperatures (Robinson et al. 2023).

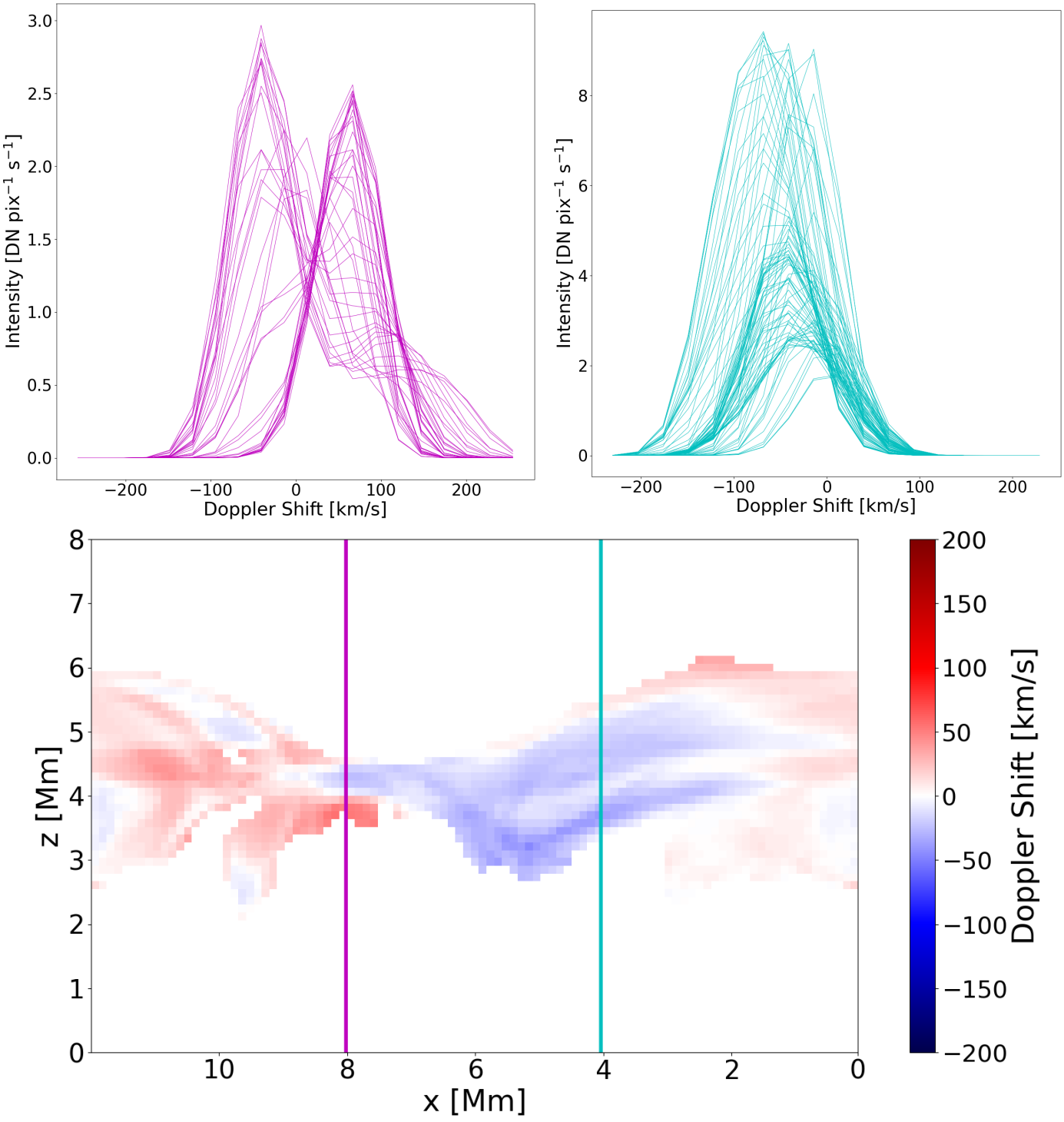

Fig. 12. Synthetic MUSE spectra along vertical cuts at $x \approx 4$ and 8 Mm at $t = 11\,360$ s. The upper-left panel is a collection of spectra along $x \approx 8$ Mm, and the upper-right panel is the spectra along $x \approx 4$ Mm. For reference, the lower panel shows the MUSE Doppler shift as well as the locations of the cuts.

This is an example where co-observations and an associated magnetogram would help distinguish the difference between these two processes. A photospheric magnetogram still cannot directly indicate the underlying trigger mechanism, but it can give the strength of the photospheric magnetic field, which can then be used to determine the amount of free magnetic energy available. While we do have component reconnection during the buildup phase of our magnetic flux rope, the resulting plasma temperatures are not reliably detectable in Fe IX 171 Å or Fe XII 195 Å during that process. This is because the strength of the background magnetic field is far weaker in our quiet Sun simulation than in the active region observed by Hi-C.

In our simulation, we have all necessary magnetic field information for our computational box. For an observation, it helps to have as many co-observations as possible; in this

case, SDO/AIA observations as well as the associated SDO Helioseismic and Magnetic Imager (SDO/HMI; Scherrer et al. 2012) magnetogram. If the observed atmosphere is associated with an active region, then component reconnection and magnetic braiding may produce the high temperatures and EUV brightenings as observed with Hi-C. If the observed atmosphere is quiet Sun, then it is unlikely that component reconnection holds enough magnetic energy to transfer into hot plasma jets observable in EUV lines. In that case, the observed brightening would likely be a result of large-angle reconnection, as in our simulation. This example serves as a word of caution when interpreting observations, and when comparing observations to simulations. As shown here, observables with similar characteristics at similar wavelengths could be brought about by two completely different physical processes.

5. Conclusions

In this work, we present synthetic observables of a nanoflare-scale reconnection event between a magnetic arcade, a magnetic flux rope, and an overlying, nearly antiparallel field in the corona. This reconnection is a result of the gradual buildup of the magnetic flux rope in the corona and is not associated with flux emergence, cancellation, or tether-cutting reconnection. Synthetic observables of optically thin EUV lines then show how the resulting event appears when self-ordered coronal features undergo large-angle reconnection.

We have determined that such nanoflare-scale events can be seen in channel 171 of SDO/AIA, including details of the bidirectional jet systems that provide information about the magnetic topology. This event would also be visible in the 171 channel of MUSE once it is operational, and the 37-slit setup of MUSE should prove very useful when observing small-scale reconnection events such as this one.

Moving forward, it would be informative to simulate a full MUSE observable that would account for all 37 slits as well as temporal evolution. Additionally, further investigation into optically thick lines could improve our understanding of how the flux rope looks as a possible over-dense mini-filament. Since photospheric magnetograms are not as useful when the relevant magnetic features build up in the corona, observing (or synthesizing) several different optically thin and thick lines could provide necessary context to small-scale events, leading to a much more comprehensive and detailed story. For now, we argue that nanoflare-scale reconnection events, which can impulsively heat the corona, are possible to observe and describe as long as we have sufficient instruments to resolve them and adequate context from numerical simulations.

Acknowledgements. R.A.R. wishes to acknowledge Juan Martínez-Sykora for the scripts and MUSE response functions necessary for calculating synthetic observables, as well as support and expertise from Mikołaj Szydlarski and Helle Bakke. She also thanks Guillaume Aulanier and Bart De Pontieu for their insight regarding mini-filaments. This research was supported by the Research Council of Norway through its Centres of Excellence scheme, project number 262622. Computational resources have been provided by Sigma2 – the National Infrastructure for High-Performance Computing and Data Storage in Norway. We acknowledge funding support by the European Research Council under ERC Syngergy grant agreement No. 810218 (Whole Sun).

References

Antolin, P., Pagano, P., Testa, P., Petralia, A., & Reale, F. 2021, Nat. Astron., 5, 54
Aulanier, G. 2014, in Nature of Prominences and their Role in Space Weather, eds. B. Schmieder, J. M. Malherbe, & S. T. Wu, 300, 184
Bahauddin, S. M., Bradshaw, S. J., & Winebarger, A. R. 2021, Nat. Astron., 5, 237
Bakke, H., Carlsson, M., Rouppe van der Voort, L., et al. 2022, A&A, 659, A186
Bello González, N., Danilovic, S., & Kneer, F. 2013, A&A, 557, A102
Berghmans, D., Auchere, F., Zhukov, A., et al. 2021, AGU Fall Meeting Abstracts, 2021, SH21A–02
Boerner, P., Edwards, C., Lemen, J., et al. 2012, Sol. Phys., 275, 41
Carlsson, M., & Leenaarts, J. 2012, A&A, 539, A39
Chen, Y., Przybylski, D., Peter, H., & Tian, H. 2021, EGU General Assembly Conference Abstracts, EGU General Assembly Conference Abstracts, EGU21–5061
Cheung, M. C. M., Martínez-Sykora, J., Testa, P., et al. 2022, ApJ, 926, 53
Cirtain, J. W., Golub, L., Winebarger, A. R., et al. 2013, Nature, 493, 501
De Pontieu, B., Martínez-Sykora, J., Testa, P., et al. 2020, ApJ, 888, 3
De Pontieu, B., Testa, P., Martínez-Sykora, J., et al. 2022, ApJ, 926, 52
Del Zanna, G., Dere, K. P., Young, P. R., & Landi, E. 2021, ApJ, 909, 38
Dere, K. P., Landi, E., Mason, H. E., Monsignori Fossi, B. C., & Young, P. R. 1997, A&AS, 125, 149
Druett, M. K., Leenaarts, J., Carlsson, M., & Szydlarski, M. 2022, A&A, 665, A6
Gudiksen, B. V., Carlsson, M., Hansteen, V. H., et al. 2011, A&A, 531, A154
Hahn, M., Ho, B., & Savin, D. W. 2022, ApJ, 936, 113
Hannah, I. G., Hudson, H. S., Battaglia, M., et al. 2011, Space Sci. Rev., 159, 263
Hannah, I. G., Kleint, L., Krucker, S., et al. 2019, ApJ, 881, 109
Hayek, W., Asplund, M., Carlsson, M., et al. 2010, A&A, 517, A49
Hong, J., Jiang, Y., Yang, J., et al. 2016, ApJ, 830, 60
Hyman, J. 1979, in Advances in Computer Methods for Partial Differential Equations, eds. R. Vichnevetsky, & R. S. Stepleman, Int. Assoc. Math. Comput. Simul., 442
Joshi, J., & Rouppe van der Voort, L. H. M. 2022, A&A, 664, A72
Kahil, F., Hirzberger, J., Solanki, S. K., et al. 2022, A&A, 660, A143
Kuhar, M., Krucker, S., Glesener, L., et al. 2018, ApJ, 856, L32
Lemen, J. R., Title, A. M., Akin, D. J., et al. 2012, Sol. Phys., 275, 17
Libbrecht, T., Joshi, J., de la Cruz Rodríguez, J., Leenaarts, J., & Ramos, A. A. 2017, A&A, 598, A33
Martínez-Sykora, J., De Pontieu, B., Testa, P., & Hansteen, V. 2011, ApJ, 743, 23
Martínez-Sykora, J., De Pontieu, B., De Moortel, I., Hansteen, V. H., & Carlsson, M. 2018, ApJ, 860, 116
Nóbrega-Siverio, D., & Moreno-Insertis, F. 2022, ApJ, 935, L21
Nordlund, A. 1982, A&A, 107, 1
Nordlund, Å., & Galsgaard, K. 1995, A 3D MHD Code for Parallel Computers, Tech. Rep.
Parker, E. N. 1988, ApJ, 330, 474
Pesnell, W. D., Thompson, B. J., & Chamberlin, P. C. 2012, Sol. Phys., 275, 3
Polito, V., Testa, P., Allred, J., et al. 2018, ApJ, 856, 178
Priest, E. R. 1983, Sol. Phys., 86, 33
Purkhart, S., & Veronig, A. M. 2022, A&A, 661, A149
Rempel, M. 2017, ApJ, 834, 10
Robinson, R. A., Carlsson, M., & Aulanier, G. 2022, A&A, 668, A177
Robinson, R. A., Aulanier, G., & Carlsson, M. 2023, A&A, 673, A79
Scherrer, P. H., Schou, J., Bush, R. I., et al. 2012, Sol. Phys., 275, 207
Skartlien, R. 2000, ApJ, 536, 465
Sterling, A. C., & Moore, R. L. 2016, ApJ, 828, L9
Sterling, A. C., Moore, R. L., Samanta, T., & Yurchyshyn, V. 2020, ApJ, 893, L45
Syntelis, P., & Priest, E. R. 2021, A&A, 649, A101
Testa, P., De Pontieu, B., Martínez-Sykora, J., et al. 2013, ApJ, 770, L1
Testa, P., Polito, V., & De Pontieu, B. 2020, ApJ, 889, 124
Ulyanov, A. S., Bogachev, S. A., Loboda, I. P., Reva, A. A., & Kirichenko, A. S. 2019, Sol. Phys., 294, 128
Zachariadis, T. G., Alissandrakis, C. E., & Banos, G. 1987, Sol. Phys., 108, 227
Zacharias, P., Hansteen, V. H., Leenaarts, J., Carlsson, M., & Gudiksen, B. V. 2018, A&A, 614, A110